Photoionization of Ne^+ using synchrotron radiation

A. M. Covington, A. Aguilar, I. R. Covington, M. F. Gharaibeh, G. Hinojosa,* C. A. Shirley, and R. A. Phaneuf
Department of Physics, MS 220, University of Nevada, Reno, Nevada 89557-0058

I. Álvarez and C. Cisneros
Centro de Ciencias Físicas, Universidad National Autónoma de México, Apartado Postal 6-96, Cuernavaca 62131, Mexico

I. Dominguez-Lopez,† M. M. Sant'Anna,‡ and A. S. Schlachter
Advanced Light Source, Lawrence Berkeley National Laboratory, 1 Cyclotron Road, MS 7-100, Berkeley, California 94720

B. M. McLaughlin§ and A. Dalgarno
Institute for Theoretical Atomic and Molecular Physics, Harvard Smithsonian Center for Astrophysics, 60 Garden Street, Cambridge, Massachusetts 02138

(Received 10 September 2002; published 30 December 2002)

Absolute measurements of cross sections for photoionization of a statistical admixture of Ne^+ in the $^2P^o_{3/2}$ ground state and the $^2P^o_{1/2}$ metastable state are reported in the energy range 40–71 eV at photon energy resolutions ranging from 22 meV to 2 meV. The experiments were performed using synchrotron radiation from an undulator beamline of the Advanced Light Source with a newly developed ion-photon-beam endstation. The data are characterized by multiple Rydberg series of autoionizing resonances superimposed upon a direct photoionization background cross section where some of the observed resonance line shapes show evidence of interference between the direct and indirect photoionization channels. The resonance features are assigned spectroscopically, and their energies and quantum defects are tabulated. The experimental photoionization cross sections are in satisfactory agreement with the predictions from theoretical calculations performed in intermediate coupling using the semirelativistic Breit-Pauli approximation with ten states. The resonances nearest to the ionization thresholds exhibit anomalous behavior with respect to their positions and strengths due to the presence of interloping resonances associated with higher-lying ionic states causing disruption of the regular Rydberg spectral pattern.

DOI: 10.1103/PhysRevA.66.062710 PACS number(s): 32.80.Dz

I. INTRODUCTION

Photoionization of ions is a fundamental process of importance in many high-temperature plasma environments, such as those occurring in stars and nebulas [1] and in inertial-confinement fusion experiments [2]. Quantitative measurements of photoionization of ions provide precision data on ionic structure, and guidance to the development of theoretical models of multielectron interactions. In addition, the opacity databases [3–5] that are critical to the modeling and diagnostics of hot, dense plasmas consist almost entirely of theoretical calculations performed in LS-coupling. High-resolution absolute photoionization cross-section measurements are therefore necessary to benchmark such theoretical data.

Photoionization is a bound-free process that is characterized by a direct photoionization cross section that rises from zero as a step function at the ionization threshold energy and falls off monotonically with increasing photon energy,

$$\gamma + A^{q+} \rightarrow A^{(q+1)+} + e^-. \tag{1}$$

Superimposed upon this direct photoionization cross section are series of resonances occurring at discrete photon energies corresponding to the excitation of autoionizing states,

$$\gamma + A^{q+} \rightarrow (A^{q+})^{**} \rightarrow A^{(q+1)+} + e^-. \tag{2}$$

Interference between the indirect and direct photoionization channels produces characteristic Fano-Beutler line profiles for the resonances [6], providing further insight into the electronic structure of the ion and the dynamics of the photoionization process.

The photoionization of ions has been studied experimentally by several techniques, whose main features, relative advantages, and limitations have been presented in a recent topical review by West [7]. The technique of photoion-yield spectroscopy using synchrotron radiation was pioneered by Lyon and collaborators [8] at the Daresbury synchrotron in the U.K., and involves merging ion beams accelerated to keV energies with monochromatic, tunable beams of synchrotron radiation. Photoions produced by their interaction over common paths of tens of centimeters may be magnetically or

*Present address: Centro de Ciencias Físicas, Universidad Nacional Autónoma de México, Apartado Postal 6-96, Cuernavaca 62131, Mexico.

†Present address: Centro Nacional de Metrología, Querétaro, Qro. 76900, Mexico.

‡Present address: Instituto de Física, Universidade Federal do Rio de Janeiro, Caixa Postal 68528, 21945-970 Rio de Janeiro, RJ, Brazil.

§Present address: Department of Applied Mathematics and Theoretical Physics, The Queens University of Belfast, Belfast BT7 1NN, United Kingdom.

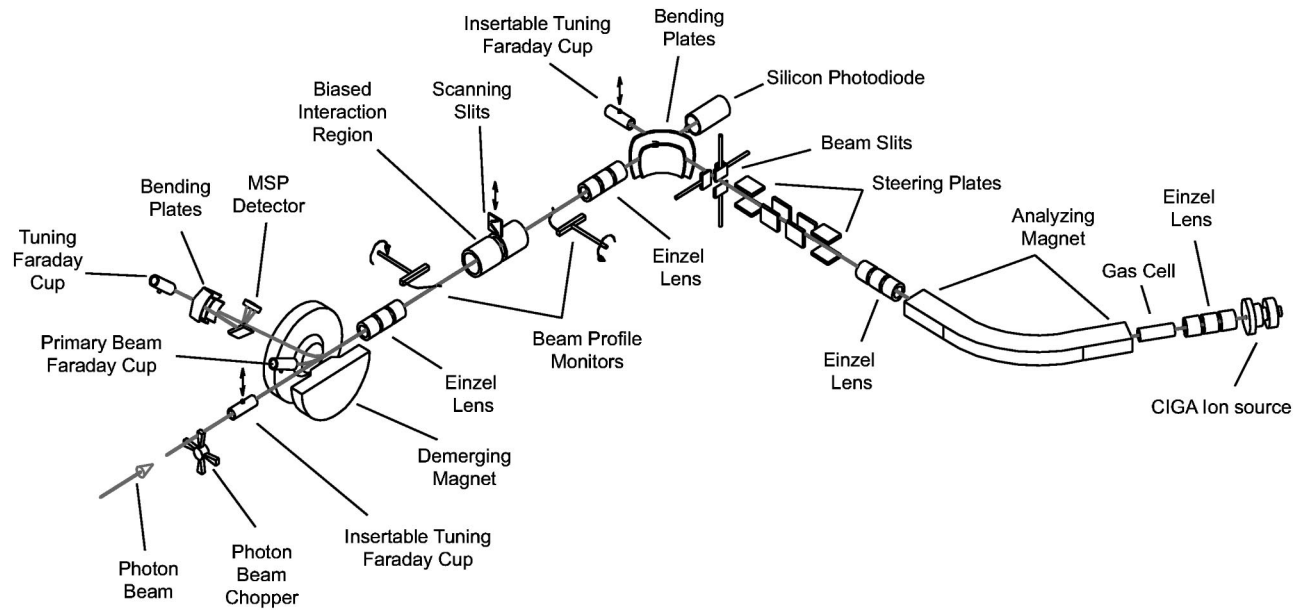

FIG. 1. Ion-photon beam (IPB) endstation installed on ALS beamline 10.0.1.2.

electrostatically separated from the parent ion beam. The directed ion beam and negligible momentum transfer permit a complete collection of the photoions. If the energy of the ion beam is not too high and ultrahigh vacuum conditions prevail, the background produced by stripping collisions of the primary ion beam with residual gas is manageable, and may be subtracted by chopping the photon beam. Furthermore, the merged-beams technique is amenable to absolute cross-section measurements [9].

Until recently, because of the relatively low density presented by a space-charge-limited ion beam ($\sim 10^6$ cm^{-3}), data for ions were limited mainly to singly charged alkali, alkaline earth, and transition-metal ions with large photoionization cross sections [7]. The advent of third-generation synchrotron radiation sources with insertion devices has increased the photon beam intensities available to experimenters by nearly three orders of magnitude, making possible the study of photoionization of ions with unprecedented sensitivity and spectral resolution. This has permitted measurements with ions of the lighter and more astrophysically abundant elements, e.g., C^+ [10], O^+ [13,12] and more recently C^{2+} [14], which are helping to refine theoretical descriptions of the photoionization process.

Neon, being the sixth most abundant element in the universe, is of considerable importance in astrophysics. The ions of neon are of interest due to their role in interpreting the observations of astronomical objects such as gaseous nebulas. At ultraviolet wavelengths in the range 300–90 Å, corresponding to a photon energy range of 41–138 eV, radiation can photoionize the ground states of several ionization stages of neon such as Ne^+, Ne^{2+}, Ne^{3+}, and Ne^{4+}, leaving the residual ion in one of several excited states. These ions of neon, together with those of carbon (C^{2+}, C^{3+}, C^{4+}), nitrogen (N^{2+}, N^{3+}, N^{4+}), and oxygen (O^{2+}, O^{3+}, O^{4+}) contribute to the opacity in the atmospheres of the central stars of planetary nebulas [15,16]. In this paper, both high-resolution absolute measurements and theoretical calculations are presented for photoionization of Ne^+ at photon energies ranging from the photoionization threshold to 70 eV.

II. EXPERIMENT

The experiments were conducted at undulator beamline 10.0.1.2 of the Advanced Light Source (ALS) at Lawrence Berkeley National Laboratory. An ion-photon-beam (IPB) endstation was developed at the University of Nevada, Reno based on the merged-beams technique and photoion spectroscopy using tunable synchrotron radiation. Initial measurements of photoionization of O^+ ions [13] and C^{2+} ions [14] using the IPB endstation have already been reported briefly. The experimental method, which will be described in more detail here, is similar to that pioneered by Lyon *et al.* [8] and applied more recently by Kjeldsen *et al.* [10] and Oura *et al.* [11]. A schematic diagram of the IPB endstation is presented in Fig. 1.

A. Photon beam

The photon beam was produced by a 10-cm period undulator installed in the 1.9 GeV electron storage ring to serve ALS Beamline 10.0.1. A grazing-incidence spherical-grating monochromator delivered a highly collimated photon beam of spatial width less than 1 mm and divergence less than 0.5°. The beamline produces a photon flux of 5×10^{12} photons per second in a bandwidth of 0.01% at an energy of 40 eV. Three gratings cover the energy range 17–340 eV. Spectral resolving powers $E/\Delta E$ as high as 40 000 are available at reduced photon flux. All measurements with Ne^+ were carried out with a gold-surfaced spherical grating ruled at 380 lines/mm. The photon energy was scanned by rotating the grating and translating the exit slit of the monochromator while simultaneously adjusting the undulator gap to maximize the beam intensity. The spectral resolution was preselected by adjusting the entrance and exit slits of the mono-

chromator. The photon flux was measured by an absolutely calibrated silicon x-ray photodiode, and was typically $(2-3)\times 10^{13}$ photons/second at a nominal spectral resolving power of 2000. The analog output from a precision current meter was directed to a voltage-to-frequency converter, which provided a normalization signal to the personal-computer-based data acquisition system. The photon beam was mechanically chopped at 0.5 Hz using a stepping-motor controlled paddle to separate photoions from background produced by stripping of the parent ion beam on residual gas in the ultrahigh vacuum system. The photon energy scale was calibrated using measurements [13] of the well-known O^+ ground-state (^4S) and metastable-state (^2P and ^2D) energy thresholds, allowing for the Doppler shift due to the ion motion in the laboratory frame. The absolute uncertainty in the photon energy scale is estimated to be ± 5 meV.

B. Ion beam

$^{20}Ne^+$ ions were produced by the Cuernavaca Ion Gun Apparatus (CIGA) in a hot-filament, low-pressure discharge-type ion source, and accelerated to an energy of 6 keV. The ion beam was focused by a series of cylindrical electrostatic einzel lenses. A Ne^+ beam was selected by a 60° analyzing magnet with a mass resolution of 100. The ion beam trajectory and its cross-sectional area were defined by adjustable horizontal and vertical beam slits located downstream of the analyzing magnet. The collimated Ne^+ beam was typically a few mm in diameter, with a current in the range 50–200 nA. Three stages of differential pumping with turbomolecular pumps and a cryopump assured a downstream vacuum in the 10^{-10} Torr range.

C. Merger and beam interaction region

A pair of 90° spherical-sector bending plates merged the ion beam onto the axis of the counterpropagating photon beam. Finetuning of the overlap of the beams was achieved with two sets of mutually perpendicular electrostatic steering plates mounted immediately before the merger plates. A cylindrical einzel lens focused the beam in the center of the interaction region, which consisted of an isolated stainless-steel-mesh cylinder to which an electrical potential (typically $+2$ kV) was applied, thereby energy labeling photoions produced in this region. Series of entrance and exit apertures accurately defined the effective length (29.4 cm) of the interaction region. Two-dimensional intensity distributions of both beams were measured by commercial rotating-wire beam profile monitors installed just upstream and downstream of the interaction region, and by a translating-slit scanner located in the middle of the region. The profile monitors permitted the positions and spatial profiles of the two beams to be continuously monitored on an oscilloscope while tuning the beams. Two 500 l/s mag-ion pumps assured ultrahigh vacuum conditions in this region when the photon and ion beams were present.

D. Demerger and ion charge analyzer

A 45° dipole analyzing magnet located downstream of the interaction region separated the Ne^{2+} products from the parent Ne^+ beam, which was collected in an extended Faraday cup. The magnetic field was set such that the Ne^{2+} product ions passed through an aperture in the back of the Faraday cup. A spherical 90° electrostatic deflector directed them onto a stainless steel plate biased at -550 V, from which secondary electrons were accelerated and detected by a microsphere-plate electron multiplier used in a pulse-counting mode. The deflection planes of the demerger magnet and this spherical deflector were orthogonal, permitting the Ne^{2+} products to be swept across the detector in mutually perpendicular directions, providing a diagnostic of their complete collection. To this end, a cylindrical einzel lens located downstream of the interaction region provided a further diagnostic, but was found to be unnecessary and was turned off during the measurements. The absolute efficiency of the photoion detector was calibrated using an averaging subfemtoampere meter to record the photoion current, which was compared with the measured photoion count rate. The Ne^+ ion beam current was measured by a precision current meter, whose analog output was directed to a voltage-to-frequency converter, providing a normalization signal to the data acquisition system.

III. THEORY

Previous photoionization cross-section calculations for singly charged neon have been carried out only within the confines of LS coupling [16–18]. In order to assist the experimental endeavour in locating and concentrating high-resolution measurements in specific energy regions containing resonances, photoionization cross-section calculations were initially performed for this complex in LS-coupling using the R-matrix method [19]. With this approach, one optimizes beam time, since coarse energy scans may be carried out in resonance-free regions, allowing for the concentration of energy scans at high resolution in regions where dense resonance structure is located. This approach enabled a wealth of prominent Rydberg series of resonances to be experimentally located and analyzed with high energy resolution. In the theoretical work the $n=2$ states of Ne^{2+}, namely; $1s^2 2s^2 2p^4\ ^3P, ^1D, ^1S$, $1s^2 2s 2p^5\ ^{1,3}P^o$, and $1s^2 2p^6\ ^1S$ were included. Direct comparison of initial LS coupling results for the photoionization cross section with experiment indicated the presence of additional Rydberg series of resonances in the experimental spectral scans, demonstrating that this level of approximation was inadequate. A more accurate description required the incorporation of relativistic effects into the theoretical work. This was further illustrated by the doublet nature of the peaks in the spectral scans for the photoion yield where the separation between them is similar to that of the fine-structre splitting of the $Ne^+\ 1s^2 2s^2 2p^5\ ^2P^o_{3/2,1/2}$ levels.

Photoionization cross-section calculations for this ion were then extended to incorporate relativistic effects and performed in intermediate coupling, within the confines of the semirelativistic Breit-Pauli approximation. In the semirelativistic R-matrix calculations the same six states $1s^2 2s^2 2p^4\ ^3P$, ^1D, ^1S, $1s^2 2s 2p^5\ ^{1,3}P^o$, and $1s^2 2p^6\ ^1S$, of the Ne^{2+} ion core were employed that were retained in the

close-coupling expansions. For the Ne^{2+} product ion the orbital basis set was limited to $n=3$ in constructing the multiconfiguration interaction wave functions used to describe the six target LS states in the calculations. The Breit-Pauli R-matrix approach was then used to calculate the ten (LSJ) ion state energies of Ne^{2+} arising from these six LS states, and the photoionization cross sections determined for both the $^2P^o_{3/2}$ ground and the metastable $^2P^o_{1/2}$ initial states of the Ne^+ ion.

The photoionization cross sections for both of the initial states were determined in intermediate coupling (LSJ) using the International R-Matrix/Opacity, Iron Project, and RmaX Project programs [20–22] with the scattering wave functions generated by allowing for double electron promotions out of the base $1s^22s^22p^5$ configuration of Ne^+ into the orbital set employed. All the scattering calculations were performed with twenty continuum basis functions and a boundary radius of 11.8 bohrs. In the case of the $^2P^o_{3/2}$ initial ground state, the dipole selection rule requires the dipole transition matrices $3/2^o \rightarrow 1/2^e, 3/2^e, 5/2^e$, to be calculated, whereas for the metastable $^2P^o_{1/2}$ inital state, the dipole matrices for the transitions, $1/2^o \rightarrow 1/2^e, 3/2^e$, only are required. The Hamiltonian matrices for the $1/2^o$, $3/2^o$, $5/2^e$, $3/2^e$ and $1/2^e$ symmetries were then calculated, where the entire range of LS matrices that contribute to these $J\pi$ symmetries was used. For both the $^2P^o_{3/2}$ ground and the metastable $^2P^o_{1/2}$ initial states the outer region electron-ion collision problem [23,24] was then solved using a suitably fine energy mesh of 0.136 meV so that the fine resonance structure in the respective photoionization cross sections was fully resolved.

To analyze resonances found in the theoretical cross sections the Quigley-Berrington (QB) method [25] was used. This approach exploits the analytical properties of the R matrix to obtain the energy derivative of the reactance (**K**) matrix and has previously proved successful in locating resonances found in the cross sections for multichannel electron scattering by atomic [26] or molecular [27] systems.

IV. RESULTS

A. Absolute cross-section measurements

Absolute measurements of photoionization cross sections were performed at a number of discrete photon energies where there were no resonant features in the photoion-yield spectra. At each such photon energy $(h\nu)$, the value of the total absolute photoionization cross section σ_{pi} in cm^2 was determined from experimentally measured parameters,

$$\sigma_{pi}(h\nu) = \frac{Rqe^2 v_i \epsilon}{I^+ I^\gamma \Omega \delta \Delta \int F(z)dz}, \tag{3}$$

where R is the photoion count rate (s^{-1}), q is the charge state of the parent ion, $e=1.6\times10^{-19}$ C, v_i is the ion beam velocity (cm/s), ϵ is the responsivity of the photodiode (electrons/photon), I^+ is the ion beam current (A), I^γ is the photodiode current (A), Ω is the photoion collection efficiency, δ is the pulse transmission fraction of the photoion detection electronics (determined by the pulse-discriminator setting), Δ is the measured absolute photoion detection efficiency, and the beam overlap integral $\int F(z)dz$ defines the spatial overlap of the photon and ion beams along the common interaction path in units of cm^{-1}. The propagation direction of the ion beam is defined as the z axis. At each of the three positions z_i at which beam intensity profiles were measured, the form factor $F(z_i)$ was determined by the following relation:

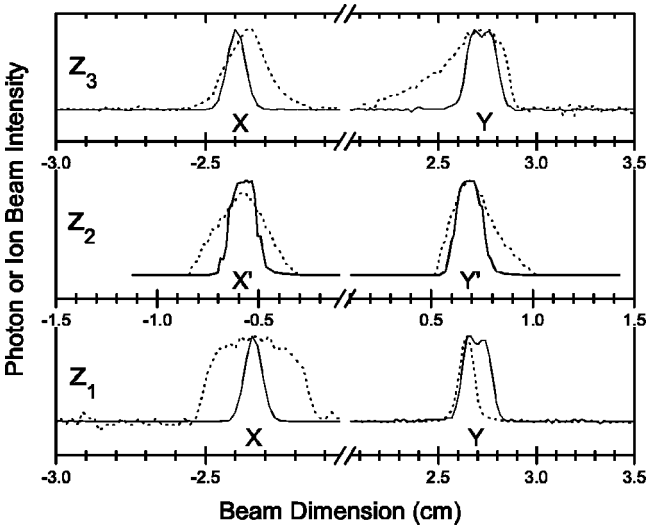

FIG. 2. Two-dimensional intensity profiles of the photon beam (solid curves) and ion beam (dashed curves) measured at three points z_i along the merged path of the beams. The measurements at z_1 and z_3 were made with rotating-wire beam-profile monitors upstream and downstream of the interaction region, and that at z_2 with the slit scanner in the center of the interaction region. The profiles correspond to the parameters in Table I.

$$F(z_i) = \frac{\int\int I^+(x,y) I^\gamma(x,y) dxdy}{\int\int I^+(x,y)dxdy \int\int I^\gamma(x,y)dxdy}. \tag{4}$$

Typical two-dimensional photon and ion beam spatial intensity profiles are shown in Fig. 2. The profiles were measured at each of the three positions z_i and form factors $F(z_i)$ were calculated using Eq. (4). The beam overlap integral in Eq. (3) was then determined by interpolation of the $F(z_i)$ to obtain $F(z)$, as illustrated in Fig. 3, and integrating along the length of the biased interaction region. Since one-dimensional rather than two-dimensional beam intensity profiles were measured, the approximation [28] was made that $I^+(x,y) = I^+(x)I^+(y)$ and $I^\gamma(x,y) = I^\gamma(x)I^\gamma(y)$. In Table I, operating parameters are given for the absolute cross-section measurement at a photon energy of 45 eV. Systematic uncertainties are presented in Table II.

Table III presents the absolute photoionization cross-section measurements along with their relative and absolute uncertainties, and the total uncertainties (their quadrature sum) estimated at the 90% confidence level. These data are plotted in Fig. 4 with error bars representing their total uncertainties. Photon energy scans taken over the energy range

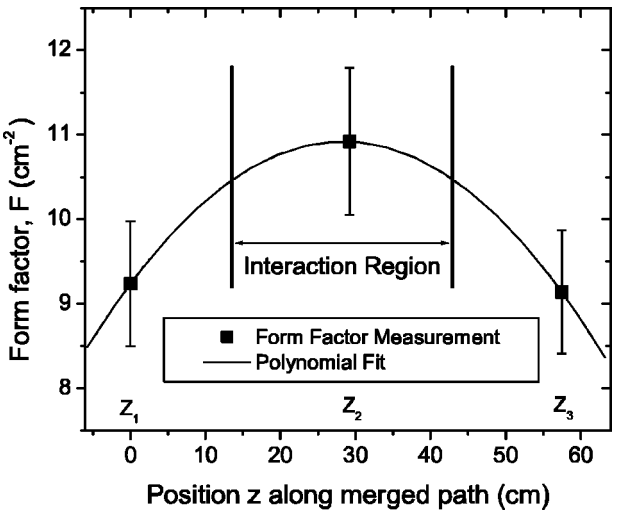

FIG. 3. Interpolation of measured form factors to characterize the spatial overlap of the photon and ion beams in the interaction region. The form factors correspond to beam-profile measurements in Fig. 2.

40–70 eV with a resolution of 22 meV and 4 meV steps were normalized to these absolute measurements by fitting a polynomial to their measured ratio as a function of energy. These data are presented in Fig. 4 as small circles connected by lines. A rich resonance structure is evident in these data, which was analyzed in detail. The resonance near 56.5 eV exhibits a markedly asymmetic profile, indicating that the direct and indirect photoionization channels are strongly interfering.

Figure 5 presents the measured cross section in the region of the $^2P_{3/2}$ ground-state and $^2P_{1/2}$ metastable-state ionization threshold energies at 40.963 eV and 40.866 eV, respectively [29]. The ratio of the magnitudes of the two threshold cross-section steps is 2.06 ± 0.10, consistent with a statistical

TABLE I. Values of experimental parameters for the Ne^+ absolute photoionization cross-section measurement at 45.0 eV.

Parameter	Value(s)
Ion beam energy	6.0 keV
Ion beam current, I^+	57.0 nA
Photon energy, $h\nu$	45.0 eV
Photodiode current, I^γ	69.5 μA
Photon flux	5.6×10^{13} photons/s
Interaction bias voltage, V_{int}	+2.0 kV
Ion interaction velocity, v_i	1.96×10^7 cm/s
Ne^{2+} signal rate, R	259 s^{-1}
Ne^{2+} background rate	50 s^{-1}
Form factors: $F(z_1),F(z_2),F(z_3)$	9.24, 10.92, 9.14 cm^{-2}
Photodiode responsivity, ϵ	7.81 electrons/photon
Merge-path length, L	29.4 cm
Pulse transmission fraction, δ	0.74
Photoion collection efficiency, Ω	1.00
Photoion detection efficiency, Δ	0.215
Cross section, σ	6.96×10^{-18} cm^2

TABLE II. Systematic uncertainties in absolute cross-section measurements estimated at 90% confidence level.

Source	Relative (%)	Absolute (%)	Total (%)
Counting statistics	2		2
Photoion detector efficiency		5	5
Photoion collection efficiency	2	2	3
Pulse counting efficiency		3	3
Primary ion collection efficiency		2	2
Ion current measurement		2	2
Photodiode responsivity	3	6	7
Photodiode current measurement	2	2	3
Beam profile measurement	3	7	8
Beam overlap integral	10	7	12
Interaction length		2	2
Quadrature sum	11	14	18

population of ground- and metastable-state ions in the primary ion beam. The present measurements are therefore considered to correspond to a sum of the ground-state cross section multiplied by 2/3 and the metastable-state cross section multiplied by 1/3. The presence of the metastable component adds complexity to the observed resonance structure and to its interpretation. The small offset of the measured cross section from zero below the $^2P_{1/2}$ threshold is attributed to the presence of higher-order radiation, which is estimated to comprise 6% of the total photon flux in this energy region.

B. Resonance structure

Previous photoionization measurements by Caldwell and co-workers [30,31] on atomic fluorine, which is isoelectronic to Ne^+, are relevant to the interpretation of the resonance

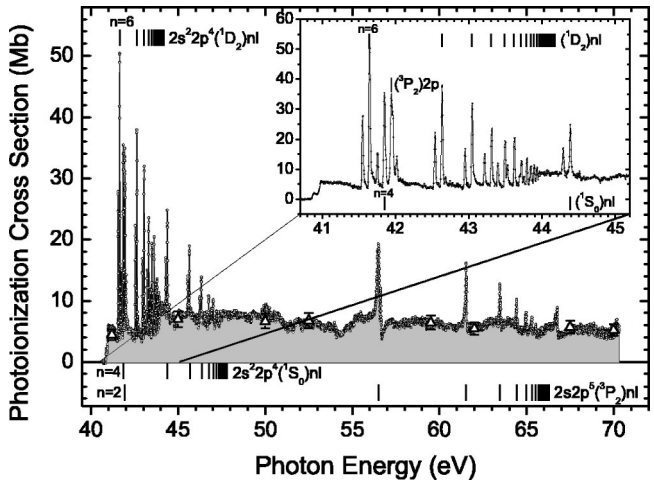

FIG. 4. Absolute cross-section measurements for photoionization of Ne^+ (triangles with error bars), to which a broad photon energy scan taken at a resolution of 22 meV and step of 4 meV has been normalized (open circles joined by lines). Three Rydberg series of resonances converging to excited states of Ne^{2+} are identified. The inset shows the low-energy region on an expanded energy scale.

TABLE III. Measured values of the total absolute cross sections for photoionization of Ne^+.

Energy (eV)	Cross section (10^{-18} cm^2)	Relative uncertainty (10^{-18} cm^2)	Absolute uncertainty (10^{-18} cm^2)	Total uncertainty (10^{-18} cm^2)
41.2	4.45	0.50	0.65	0.82
45.0	6.96	0.78	1.01	1.27
50.0	6.67	0.75	0.97	1.22
52.5	6.76	0.76	0.98	1.24
59.5	6.44	0.72	0.93	1.18
62.0	5.48	0.61	0.79	1.00
67.5	5.69	0.64	0.83	1.04
70.0	5.23	0.59	0.76	0.96

structure in the present experiment. They employed photoelectron spectrometry to map out the autoionizing resonances above the photoionization threshold. In the Ne^+ measurements, resonance structure approximately 0.5 eV above the photoionization thresholds is evident in Fig. 4, and highlighted in the inset. Because of the dense resonance structure, this energy region was studied at an increased photon energy resolution of 11 meV. These data are presented in Fig. 6 along with the theory and the assignments of the observed features. Except for a downward energy shift of 70 meV for the pair of $2s^22p^4(^1D_2)6l$ resonances from the metastable and ground states, and an apparent underestimation of the relative strength of the $2s^22p^4(^1S_0)4l$ resonances, the theory reproduces the measurements rather well. The level of agreement is encouraging, considering that resonances from three different electron core configurations occur within an energy span of less than 0.5 eV.

The $2s^22p^4(^1D_2)ns,nd$ resonances due to indirect photoionization from the $^2P^o_{3/2}$ ground state of Ne^+ converge to a series limit at 44.167 eV [32], while those from the $^2P^o_{1/2}$ metastable state have their limit at 44.070 eV. Figure 7 shows a comparison with theory of the high-n portions of these two Rydberg series measured at a higher photon energy resolution of 7.5 meV. The ns and nd components are not resolved by the experiment or the calculation. Although several of the higher-n resonances arising from the metastable and ground states of Ne^+ overlap in energy, most members of these interleaved Rydberg series are assignable for principal quantum numbers $n \leqslant 25$.

Evident in Fig. 4 are series of resonances converging to a limit of 47.875 eV from the ground state, and to 47.778 eV from the metastable state of Ne^+. Based on the analysis of Caldwell and Krause [30] for F, these narrow resonances are attributed to the $2s^22p^4(^1S_0)nd$ Rydberg series. The signature of the $2s^22p^4(^1S_0)ns$ Rydberg series in the measurements on F was a series of broad window resonances that were clearly evident in their data. Broad window resonances may be responsible for the apparent structure in the Ne^+ continuum cross section in the 44–48 eV energy range. The assignment of such broad features is complicated by the ad-

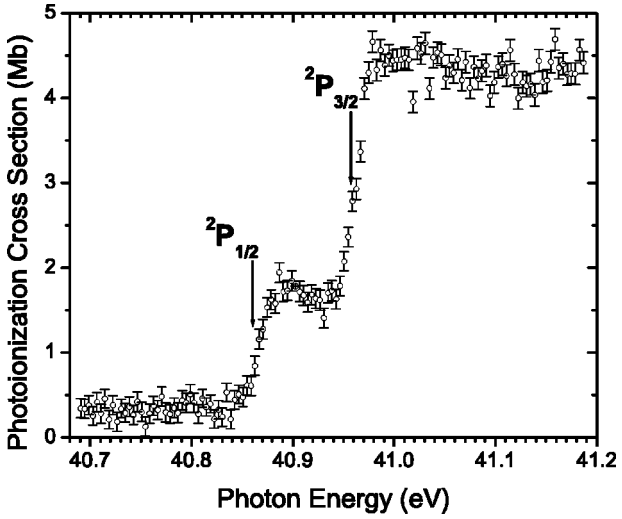

FIG. 5. Photoionization measurements at 22 meV resolution in the energy region of the $^2P_{3/2}$ ground-state and $^2P_{1/2}$ metastable-state ionization thresholds of Ne^+ at 40.963 eV and 40.866 eV, respectively. The small, nonzero cross section at energies below both thresholds is attributed to higher-order radiation in the photon beam.

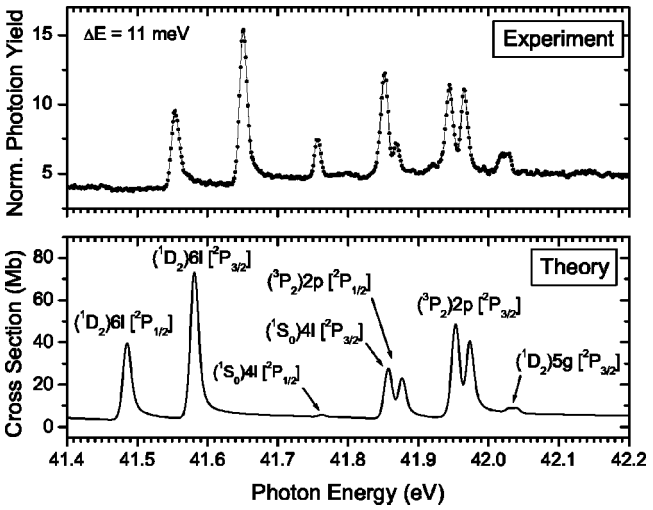

FIG. 6. Comparison of photoion yield measurements just above the Ne^+ photoionization threshold taken at an increased photon energy resolution of 11 meV with the theory. The latter has been convoluted with a Gaussian of 11 meV to simulate the experimental resolution. Members of seven Rydberg series of resonances originating from the metastable and ground states of Ne^+ are assigned.

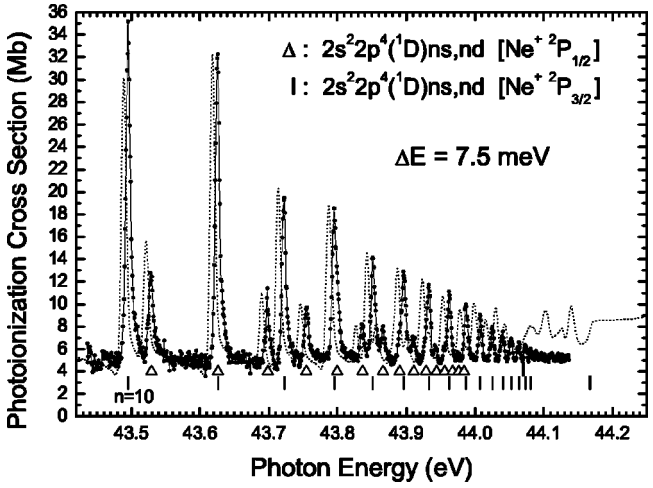

FIG. 7. Comparison of normalized Ne^+ photoionization measurements (points) taken at an energy resolution of 7.5 meV with the Breit-Pauli *R*-matrix theoretical calculation, convoluted with a Gaussian energy distribution of the same width (dotted curve). Assignments are indicated for two distinct Rydberg series of resonances due to $2p \rightarrow ns,nd$ excitation from the metastable and ground states.

mixture of metastable and ground-state ions, and was unsuccessful. Because of the uncertainty in assignment, this Rydberg series is designated hereafter by $2s^2 2p^4(^1S_0)ns,nd$.

The $2s2p^5(^3P_2)np$ Rydberg series of broad resonances from the ground state converging to a limit of 66.292 eV is also observable in the data of Fig. 4. In this case, the metastable and ground-state components are unresolved, with the exception of the resonances attributed to $2s2p^6$ between 41.8 and 42.0 eV in the scan at 11 meV resolution shown in Fig. 6. A resonance at 66.74 eV, attributed to the $2s2p^5(^1P)ns,nd$ series, occurs just above the $^3P_2$ series limit.

The energies of the observed resonances, their assignments, and their calculated quantum defects are presented in Table IV. The quantum defects are based on $\mathrm{Ry}(Ne^+) = 13.6053\ \mathrm{eV} \times 2^2$ and the known series limits obtained from tabulated Ne^2+ energy levels [29]. The quantum defects for the $2s^2 2p^4(^1S_0)ns,nd$ series are uniformly close to unity, consistent with an assignment of ns. However, as noted, Caldwell *et al.* [31] assign the the corresponding series of sharp resonances in photoionization of F as nd.

An interesting feature of these data is the nearly monotonic decrease of the quantum defects for the $2s^2 2p^4(^1D_2)ns,nd$ series from both the ground-state and the metastable state of Ne^+. These two series of narrow resonances are the best characterized experimentally, and encompass the broadest range of *n* values. One might suspect a systematic error in the photon energy calibration, were it not for the fact that the two $2s^2 2p^4(^1S_0)nd$ series overlap the same energy range and exhibit stable quantum defects. Assignment of the series limit might also be suspect, but a fit to the observed resonance energies as a function of *n* with the series limit as a free parameter gives a value of 44.165 ± 0.005 eV, compared to the spectroscopic reference value of 44.167 eV [29].

Another interesting question concerns the assignment of the $2s^2 2p^4(^3D)6s,6d$ and $2s^2 2p^4(^1S)4s,4d$ resonances that are within 0.2 eV of one another. Their assignments indicated in Table IV and Fig. 6 give quantum defects that are inconsistent with the higher-*n* members of these series, as shown in Fig. 8 for the $2s^2 2p^4(^3D)ns,nd$ series. However, their resonance strengths compare as expected to higher-*n* members of the series. Exchanging the $2s^2 2p^4(^3D)6s,6d$ and $2s^2 2p^4(^1S)4d$ assignments makes their quantum defects more consistent, but their resonance strengths become anomalous. Because of this apparent inconsistency, their assignments are uncertain and are quoted in parentheses in Table IV.

C. Resonance line shapes and widths

The properties of two observed resonance features that correspond only to photoionization of ground-state Ne^+ were studied in more detail by recording them at increasing photon energy resolution and fitting the measured line shape to a modified Fano-Beutler profile [6] of the form

$$\sigma = \sigma_0 \left\{ 1 - \rho^2 + \rho^2 \frac{(q+\epsilon)^2}{1+\epsilon^2} \right\}, \tag{5}$$

where σ_0 is the part of the photoionization cross section that corresponds to transitions to continuum states that do not interact with the discrete autoionizing state, ρ and q are numerical line profile indices, and $\epsilon = 2(h\nu - E_0)/\Gamma$, where $h\nu$ is the photon energy, E_0 is the resonance energy, and Γ is its full energy width at half maximum (FWHM). A typical fit of Eq. (5) to the $2s^2 2p^4(^1D_2)6l$ experimental resonance is shown in Fig. 9. The slight departure of the measured line shape from the Fano-Beutler profile is attributed to the influence of nearby resonances.

Figure 10 shows the results of similar fits to the $n=6$ (triangles) and $n=10$ (circles) members of the $2s^2 2p^4(^1D_2)ns,nd$ Rydberg series plotted versus the nominal photon energy resolution set by the entrance and exit slits of the monochromator. The dotted line is a linear fit of the three $n=6$ data points at highest resolution, and indicates a natural linewidth of 5.1 ± 0.3 meV. For the $n=10$ resonance, the linewidth estimated from a linear fit to the data is 2.3 $(+0.7, -0.2)$ meV. Included in Fig. 10 are the theoretical results for the natural linewidths of the same resonances via the QB method [25–27]. The theoretical values of 4.74 meV for $n=6$ and 2.28 meV for $n=10$ are consistent with the measurements.

D. Comparison between absolute cross-section measurements and theory

The absolute photoionization cross-section measurements taken at an energy resolution of 22 meV are compared in Fig. 11 with the results of the *ab initio* Breit-Pauli *R*-matrix theoretical calculation. The calculation represents a sum of the cross sections for photoionization from the ground and metastable states weighted by their statistical weights (2/3 and 1/3, respectively). A Gaussian of 22 meV FWHM was con-

TABLE IV. Principal quantum numbers n, resonance energies, and quantum defects δ determined from the measurements. The uncertainties in the experimental energies are estimated to be ± 0.005 eV for the $2s^2 2p^4(^1D_2)ns,nd$ and $2s^2 2p^4(^1S_0)ns,nd$ series, and ± 0.010 eV for the $2s2p^5(^3P_2)np$ series. The spectral assignments are uncertain for entries in parentheses. Entries in square brackets are tabulated values for transitions to bound states [29].

Initial state	n	Rydberg series $2s^2 2p^4(^1D_2)ns,nd$ Energy (eV)	δ	Rydberg series $2s^2 2p^4(^1S_0)ns,nd$ Energy (eV)	δ	Rydberg series $2s2p^5(^3P_2)np$ Energy (eV)	δ
$2s^2 2p^5\,^2P_{3/2}$	2					41.943	0.50
	3	[37.969]3*d*		[34.304]3*s*		56.490	0.64
	4			(41.852)	(0.99)	61.515	0.62
	5			44.383	1.05	63.459	0.62
	6	(41.650)	(1.35)	45.650	1.05	64.420	0.61
	7	42.636	1.04	46.335	1.06	64.956	0.62
	8	43.047	1.03	46.746	1.06	65.294	0.62
	9	43.311	1.03	47.014	1.05	65.520	0.60
	10	43.494	1.01	47.196	1.05	65.673	0.62
	11	43.627	0.96	47.326	1.04	65.786	0.63
	12	43.723	0.93	47.425	1.00	65.874	0.59
	13	43.796	0.89	47.499	0.97		
	14	43.851	0.88	47.552	1.02		
	15	43.896	0.83	47.595	1.06		
	16	43.932	0.78				
	17	43.963	0.67				
	18	43.986	0.66				
	19	44.007	0.56				
	20	44.025	0.42				
	21	44.041	0.22				
	22	44.053	0.15				
	23	44.063	0.12				
	24	44.073	−0.06				
	25	44.080	−0.01				
	∞[a]	44.167		47.875		66.292	
$2s^2 2p^5\,^2P_{1/2}$	4			(41.757)	(0.99)		
	5			44.287	1.05		
	6	(41.554)	(1.35)	45.552	1.06		
	7	42.539	1.04	46.238	1.06		
	8	42.951	1.03	46.650	1.05		
	9	43.215	1.02	46.918	1.05		
	10	43.399	0.99	47.098	1.05		
	11	43.528	0.98	47.229	1.04		
	12						
	13	43.698	0.90	47.401	0.99		
	14	43.755	0.86	47.454	1.04		
	15						
	16	43.836	0.75				
	17	43.866	0.67				
	18						
	19	43.911	0.50				
	20						
	21	43.944	0.22				
	22						
	23						
	24	43.976	−0.06				
	∞	44.070		47.778			

[a]From NIST Standard Reference Database [29].

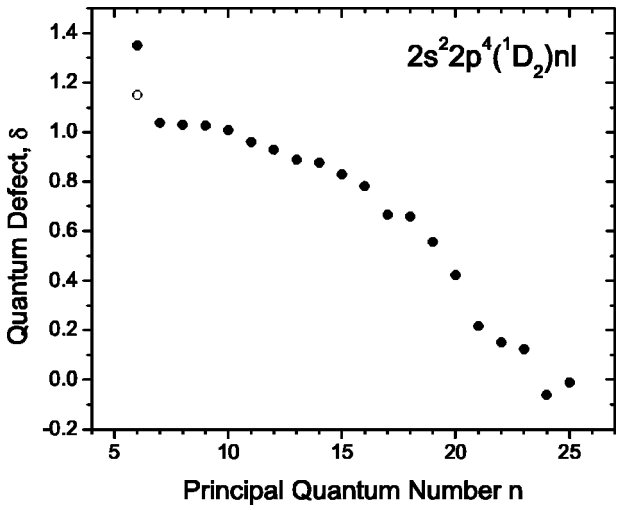

FIG. 8. Plot of quantum defects versus principal quantum number n for the $2s^22p^4(^1D_2)ns,nd$ Rydberg series from the ground state of Ne^+. The solid circles correspond to the data in Table IV, while the open circle for $n=6$ corresponds to a reversal of the assignments of the lowest-n resonances of the $2s^22p^4(^1D_2)ns,nd$ and $2s^22p^4(^1S)nd$ Rydberg series.

voluted with the theoretical data to simulate the experimental energy resolution. The calculated nonresonant cross section is almost indistinguishable from the experiment in the energy range 41–44 eV, but differs from the measurement at higher energies. As already noted, the origin of the broad structures in the measurements above 44 eV may be interleaved series of $2s2p^4(^1S)ns$ window resonances similar to but broader than those observed by Caldwell *et al.* [31] in photoionization of F. The theory predicts a small resonance just above the Ne^+ threshold that is absent in the experiment. It is noteworthy that the predicted energy of the lowest-n resonance

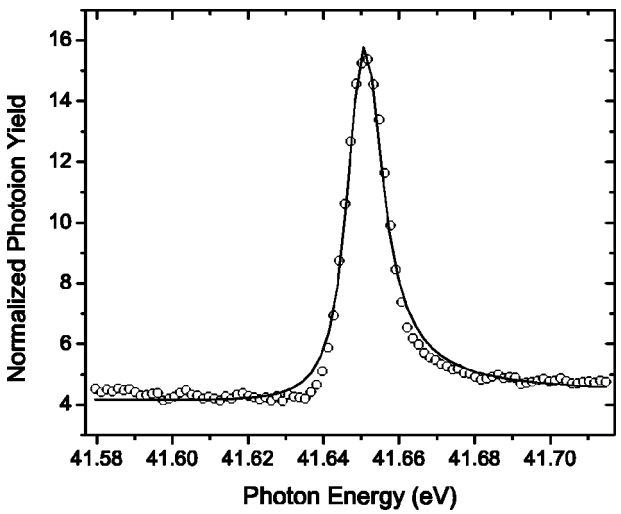

FIG. 9. Typical fit of a Fano-Beutler profile (solid line) to the experimental data points (open circles) for the $2s^22p^4(^1D_2)6s,6d$ resonance feature from ground-state Ne^+ at a photon energy resolution of 11 meV. The fit indicates a linewidth of 10.7 meV.

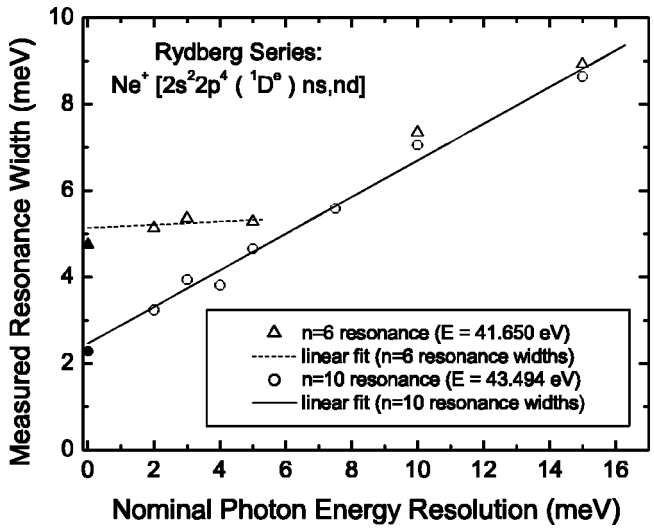

FIG. 10. Measured resonance linewidths for two members of the $2s^22p^4(^1D_2)ns,nd$ Rydberg series from the ground state of Ne^+ as functions of the photon energy resolution. The dashed line is a linear fit to the three data points at highest resolution for the $n=6$ resonance (open triangles) and indicates a natural linewidth of 5.1 ± 0.2 meV FWHM. The width obtained theoretically (4.75 meV) is indicated by a solid triangle. The solid line is a linear fit to the data points for the $n=10$ resonance (open circles), indicating a natural linewidth of $2.3(+0.7,-0.2)$ meV FWHM. The solid circle is the theoretical value of 2.28 meV.

differs from experiment by about 0.1 eV, whereas most of the higher-n resonance energies are in near-perfect agreement. The predicted energy of the $2s2p^5(^3P_2)3p$ resonance feature lies above the measured value of 56.49 eV by more than 1 eV, although the complex line shapes are similar. A predicted sharp resonance near 69 eV is absent in the experimental data.

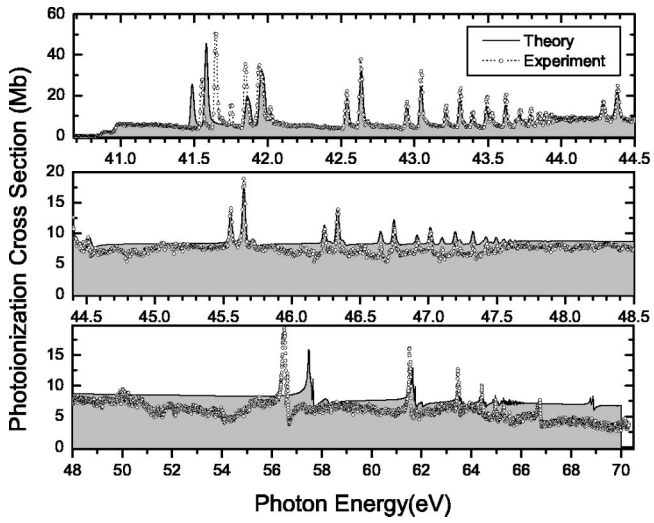

FIG. 11. Comparison of Breit-Pauli R-matrix theoretical calculation (solid line bounding shaded area) and absolute experiment (open circles) for photoionization of Ne^+. The theoretical curve has been convoluted with a Gaussian of 22 meV FWHM to simulate the photon energy bandwidth of the experiment.

V. SUMMARY

Absolute photoionization cross sections have been measured for a statistical mixture of ground-state and metastable Ne^+ in the photon energy range 40–71 eV with resolution of 22 meV. The measurements are rich in resonance structure due to indirect photoionization, and are in satisfactory agreement with an *ab initio* Breit-Pauli *R*-matrix theoretical calculation. Some of the resonance features were investigated at higher spectral resolution, and linewidths were determined for two isolated resonances. Nearly all of the observed resonance features were spectroscopically assigned, and quantum defects were determined for each. The strongest resonance features, which are closest to the ionization thresholds, exhibit anomalous behavior with respect to their strengths and energies, rendering their assignments uncertain.

ACKNOWLEDGMENTS

The experimental work was supported by the Office of Basic Energy Sciences, Chemical Sciences, Geosciences and Biosciences Division, of the U.S. Department of Energy under Grant No. DE-FG03-97ER14787 with the University of Nevada, Reno; by the Nevada DOE/EPSCoR Program in Chemical Physics; and by CONACyT through the CCF-UNAM, Cuernavaca, Mexico. A.A. and M.M.SA. acknowledge support from DGAPA-UNAM (Mexico) and CNPq (Brazil), respectively. B.M.M.C.L. would like to thank the Institute for Theoretical Atomic and Molecular Physics (ITAMP) for hospitality and support. ITAMP was supported by a grant from the National Science Foundation to Harvard University and the Smithsonian Astrophysical Observatory. A.D. acknowledges support for theoretical work from US DOE Grant No. DE-FG02-88ER13861.

[1] J.N. Bregman and J.P. Harrington, Astrophys. J. **309**, 833 (1986).
[2] I. Hofmann, Laser Part. Beams **8**, 527 (1990).
[3] W. Cunto, C. Mendoza, F. Ochsenbein, and C.J. Zeippen, Astron. Astrophys. **275**, L5 (1993).
[4] C.A. Iglesias and F.J. Rogers, Astrophys. J. **464**, 943 (1996).
[5] M.A. Bautista and T.R. Kallman, Astrophys. J., Suppl. Ser. **134**, 139 (2001).
[6] U. Fano and J.W. Cooper, Phys. Rev. **137**, A1364 (1965).
[7] J.B. West, J. Phys. B **34**, R45 (2001).
[8] I.C. Lyon, B. Peart, J.B. West, and K. Dolder, J. Phys. B **19**, 4137 (1986).
[9] R.A. Phaneuf, C.C. Havener, G.H. Dunn, and A. Müller, Rep. Prog. Phys. **62**, 1143 (1999).
[10] H. Kjeldsen, F. Folkmann, H. Knudsen, M.S. Rasmusssen, J.B. West, and T. Andersen, Astrophys. J. **524**, L143 (1999).
[11] M. Oura, S. Kravis, T. Koizumi, Y. Itoh, T.M. Kojima, M. Sano, T. Sekoika, M. Kimura, K. Okuno, and Y. Awaya, Nucl. Instrum. Methods Phys. Res. **86**, 190 (1994).
[12] H. Kjeldsen, B. Kristensen, R.L. Brooks, F. Folkmann, H. Knudsen, and T. Andersen, Astrophys. J., Suppl. Ser. **138**, 219 (2002).
[13] A.M. Covington, A. Aguilar, I.R. Covington, M. Gharaibeh, C.A. Shirley, R.A. Phaneuf, I. Álvarez, C. Cisneros, G. Hinojosa, J.D. Bozek, I. Dominguez, M.M. Sant'Anna, A.S. Schlachter, N. Berrah, S.N. Nahar, and B.M. McLaughlin, Phys. Rev. Lett. **87**, 243002 (2001).
[14] A. Müller, R.A. Phaneuf, A. Aguilar, M.F. Gharaibeh, A.S. Schlachter, I. Álvarez, C. Cisneros, G. Hinojosa, and B.M. McLaughlin, J. Phys. B **35**, L137 (2002).
[15] C.R. O'Dell, Astrophys. J. **138**, 67 (1963).
[16] M.B. Hidalgo, Astrophys. J. **153**, 981 (1968).
[17] R.J.W. Henry, Astrophys. J. **161**, 1153 (1970).
[18] A.K. Pradhan, Mon. Not. R. Astron. Soc. **190**, 5P (1980).
[19] P.G. Burke and W.D. Robb, Adv. At. Mol. Phys. **11**, 143 (1975).
[20] D.G. Hummer, K.A. Berrington, W. Eissner, A.K. Pradhan, H.E. Saraph, and J.A. Tully, Astron. Astrophys., Suppl. Ser. **279**, 298 (1993).
[21] K.A. Berrington, W. Eissner, and P.H. Norrington, Comput. Phys. Commun. **92**, 290 (1995).
[22] K. A. Berrington and N. R. Badnell (private communication).
[23] B.M. McLaughlin and K.L. Bell, J. Phys. B **33**, 597 (2000).
[24] B.M. McLaughlin, A. Daw, and K.L. Bell, J. Phys. B **35**, 283 (2002).
[25] L. Quigley and K. Berrington, J. Phys. B **29**, 4529 (1996).
[26] L. Quigley, K. Berrington, and J. Pelan, Comput. Phys. Commun. **114**, 225 (1998).
[27] C.P. Ballance, K.A. Berington, and B.M. McLaughlin, Phys. Rev. A **60**, R4217 (1999).
[28] C.C. Havener, M.S. Huq, H.F. Krause, P.A. Schulz, and R.A. Phaneuf, Phys. Rev. A **39**, 1725 (1989).
[29] W. C. Martin, J. R. Fuhr, D. E. Kelleher, A. Musgrove, L. Podobedova, J. Reader, E.B. Saloman, C. J. Sansonetti, W. L. Wiese, P. J. Mohr, and K. Olsen, NIST Atomic Spectra Database (version 2.0) (Online). Available at http://physics.nist.gov/asd (2002). National Institute of Standards and Technology, Gaithersburg, MD.
[30] C.D. Caldwell and M.O. Krause, J. Phys. B **27**, 4891 (1994).
[31] C.D. Caldwell, S. Benzaid, A. Menzel, and M.O. Krause, Phys. Rev. A **53**, 1454 (1996).
[32] W. Persson, C.-G. Wahlström, and L. Jönsson, Phys. Rev. A **43**, 4791 (1991).